

This is the peer reviewed version of the following article:

Numerical Simulation and Experimental Validation of MIG Welding of T-Joints of Thin Aluminum Plates for Top Class Vehicles / Bonazzi, Enrico; Colombini, Elena; Panari, Davide; Vergnano, Alberto; Leali, Francesco; Veronesi, Paolo. - In: METALLURGICAL AND MATERIALS TRANSACTIONS. A, PHYSICAL METALLURGY AND MATERIALS SCIENCE. - ISSN 1073-5623. - 48:1(2017), pp. 379-388. [10.1007/s11661-016-3834-7]

Terms of use:

The terms and conditions for the reuse of this version of the manuscript are specified in the publishing policy. For all terms of use and more information see the publisher's website.

19/12/2025 02:33

Numerical Simulation and Experimental Validation of MIG Welding of T-Joints of Thin Aluminum Plates for Top Class Vehicles

Enrico Bonazzi

Department of Engineering “Enzo Ferrari”, University of Modena and Reggio Emilia
Via Pietro Vivarelli 10 - int. 1 - 41125 Modena, Italy
enrico.bonazzi@unimore.it

Elena Colombini

Department of Engineering “Enzo Ferrari”, University of Modena and Reggio Emilia
Via Pietro Vivarelli 10 - int. 1 - 41125 Modena, Italy
elena.colombini@unimore.it

Alberto Vergnano

Department of Engineering “Enzo Ferrari”, University of Modena and Reggio Emilia
Via Pietro Vivarelli 10 - int. 1 - 41125 Modena, Italy
alberto.vergnano@unimore.it

Francesco Leali

Department of Engineering “Enzo Ferrari”, University of Modena and Reggio Emilia
Via Pietro Vivarelli 10 - int. 1 - 41125 Modena, Italy
francesco.leali@unimore.it

Paolo Veronesi¹

Department of Engineering “Enzo Ferrari”, University of Modena and Reggio Emilia
Via Pietro Vivarelli 10 - int. 1 - 41125 Modena, Italy
paolo.veronesi@unimore.it

ABSTRACT

The integration of experiments with numerical simulations can efficiently support a quick evaluation of the welded joint. In this work, the MIG welding operation on aluminum T-joint thin plate has been studied by

¹ Corresponding author information can be added as a footnote.

the integration of both simulation and experiments. The aim of the paper is to enlarge the global database, to promote the use of thin aluminum sheets in automotive body industries and to provide new data. Since the welding of aluminum thin plates is difficult to control due to high speed of the heat source and high heat flows during heating and cooling, a simulation model could be considered an effective design tool to predict the real phenomena. This integrated approach enables new evaluation possibilities on MIG-welded thin aluminum T-joints, as correspondence between the extension of the microstructural zones and the simulation parameters, material hardness, transient 3D temperature distribution on the surface and inside the material, stresses, strains, and deformations. The results of the mechanical simulations are comparable with the experimental measurements along the welding path, especially considering the variability of the process. The results could well predict the welding-induced distortion, which together with local heating during welding must be anticipated and subsequently minimized and counterbalance.

I. INTRODUCTION

LIGHTWEIGHT engineering is usually exploited both in mass production vehicles for fuel saving and in top class ones for enhancing performances. [1–4] The main drivers are product design, high-performance materials, and technological processes. [5–8] During last decade,[9] thanks to the improvement in the structural optimization techniques it is also possible to reduce sections of product design. In the modern automotive industry, thicknesses lower than 3 mm are widely employed for structural assemblies, as chassis or suspensions. [5–7,10–12] The use of lightweight materials could lead to fuel saving and use phase emissions abatement; nevertheless, it is often responsible for increase in the production phase impact, particularly materials processing, thus preventing the expected benefit during use. [4] Aluminum alloys have been widely chosen due to their

properties including a high stiffness to weight ratio, low density, good formability, good corrosion resistance, and recycling potential,[11,13,14] which make them the ideal lightweight materials as it allows a mass saving of up to 50 pct over competing materials in most applications. [7,10,15,16] In this background, MIG (Metal Inert Gas) welding, one of the most common joining technologies employed in the automotive industry, despite presenting high productivity and efficiency, [17–22] is affected by some major drawbacks, such as residual stresses and distortions on welded joints. [20,23,24] The high local heating [23] due to the welding torch causes a non-uniform temperature distribution, which is responsible for high thermal gradients across the joint. As a consequence, defects or even early failure of the structures may occur. [18,20] MIG welding of aluminum results is more critical compared to steel, due to the different mechanical and thermal properties of the base and filler metals, which increase the problems of distortion and weld crater size. [24]

Hence, the fine tuning of a welding operation in industry usually follows a time- and resources-consuming approach with recursive trials and errors. Instead, the prior estimation of welding deformations would be fundamental to improve product design and process control.

As a rule, an experiment is the most realistic method to test a physical phenomenon, even if measurements might introduce errors, or require advanced instruments or, simply, some quantities are unobservable. [19,25–29]

Nowadays, numerical simulations, based on finite element (FE) method, have become very useful tools for welding process design, with a plethora of software dedicated to

simulate welding, from a metallurgical and structural point of view. However, the complexity of welding process for real engineering structures makes the simulation of welding distortions and residual stresses very difficult to set up and the support of experimental activity becomes necessary. Several responses, difficult to be directly measured, like the local temperature field, the penetration of the fusion zone, the residual stresses, and deformations, have been evaluated by numerical modeling in the recent past. [18,19,21] There are basically two methods to estimate welding deformations by means of a FE analysis: calculation of the shrinkage through a simple Elastic-FE (E-FE) analysis [19,21,30] or a multiphase simulation of solid and fluid states using a Thermal-Elastic-Plastic-FE (TEP-FE) analysis. [18,21,23,31,32] The E-FE is faster than TEP-FE, but it only estimates the final distortion, and the welding parameters must to be already defined; indeed, the TEP-FE investigates both thermal and mechanical behavior (e.g., welding penetration, final distortions). [33] Consequently, in this work the TEP-FE approach has been exploited, taking into account thermal, mechanical, metallurgic, and process-related phenomena.

The simulation has been simplified by sequentially coupling the thermal and mechanical models. The first model exploits heat elements and considers the heat $Q(x, y, z, t)$ supplied by the moving welding torch simulated by a double ellipsoidal density distribution according to the Goldak model, [34] as shown in Figure 1. This model has been widely accepted in previous research to simulate MIG welding. [18,19] The double ellipsoid is positioned and oriented in the fixed reference system with a transformation

matrix from the torch reference system. The latter computes the transient and residual temperature.

The mechanical model includes the metallurgic phenomena in terms of temperature-dependent material properties, especially when phase transitions are involved.

During a welding operation, the temperature distribution in the metal parts is transient and non-linear and it can be computed in the thermal model from the energy balance equation in thermal form as follows:

$$\rho c_p \frac{\partial T}{\partial t}(x, y, z, t) = -\nabla \cdot q(x, y, z, t) + Q(x, y, z, t) \quad (1)$$

where T is the temperature at time t in the (x, y, z) position, ρ is the material density, c_p is the specific heat capacity, q is the heat flux vector and Q is the volumetric internal heat generation.

The heat flux through the metal can be modeled by the Fourier law as follows: [35]

$$q = -k \nabla \cdot T \quad (2)$$

where k is the material heat conductivity.

The boundary condition of the model considers only the heat losses by convection and radiation, computed by Newton and Stefan–Boltzmann laws as follows: [18,19]

$$q_c = -h_f(T_s - T_0) \quad (3)$$

$$q_r = -\varepsilon \sigma (T_s^4 - T_0^4) \quad (4)$$

where h_f is the convection coefficient, ε is the emissivity of the base material, σ is the Stefan-Boltzmann constant for radiation and T_0 and T_s are the room and surface temperatures.

Considering the heat source in the axis origin, the heat flux distribution has been calculated in two different ways according to the case of the front side and rear side of the torch as follows:

$$Q(x', y', z', t) = \frac{6\sqrt{3}fP}{abc\pi\sqrt{\pi}} e^{-3\left[\frac{x'^2}{a^2} + \frac{y'^2}{b^2} + \frac{z'^2}{c^2}\right]}; \quad f, c = \begin{cases} f_f, c_f & z' \geq 0 \\ f_r, c_r & z' < 0 \end{cases} \quad (5)$$

where (x', y', z') are the local coordinates in the moving reference system associated with the welding torch, f_f and f_r are the fractions of the power applied onto the front and rear quadrants, assuming $f_f + f_r = 2$. **Error! Reference source not found.** The parameters a, b, c_f and c_r define shape and dimension of the elliptical distributions.

Considering the continuity of the volumetric heat source, f factors are linked to c parameters by $f_f = 2c_f/(c_f + c_r)$ and $f_r = 2c_r/(c_f + c_r)$. The Goldak parameters can be estimated from experiments on the welding pool and finely tuned in order to match the model with them. The welding power input $P = P(t)$ is calculated as follows:

$$P = \eta IU \quad (6)$$

where η is the welding arc efficiency with respect to the input energy (0.8 in the case of MIG technology) [14]; I is the current; and U is the voltage. The Goldak double ellipsoidal model as defined by Eq. [5] and the resultant heat flux are shown in Figure 1.

The initial condition of the simulations is

$$T(x, y, z, 0) = T_0 = \text{const} \quad (7)$$

where T_0 is assumed initially uniform through the base metal and filler wire.

In order to calculate the deformations and residual stresses after the welding operation, the time history of the temperature field, resulting from the previous simulation, is processed by a mechanical model. The total strains result from three contributors:

$$\boldsymbol{\varepsilon} = \boldsymbol{\varepsilon}_e + \boldsymbol{\varepsilon}_p + \boldsymbol{\varepsilon}_{th} \quad (8)$$

where:

- the elastic strains $\boldsymbol{\varepsilon}_e$ are calculated from the stresses by the Hooke law, including the Young modulus and the Poisson ratio of the metal in the compliance matrix.
- The plastic strains $\boldsymbol{\varepsilon}_p$ are calculated by the Von Mises criteria, considering the yield stress.
- The thermal strains contribution $\boldsymbol{\varepsilon}_{th}$ considers the expansion and contraction of the metal due to temperature variations by the thermal expansion coefficient.

During the cooling phase, after the weld beads solidification, the three internal strains balance each other. Deformations are due to the residual stress after the cooling phases in the welding process.

Previous work on MIG distortions has been mainly focused on the welding of steel plates[19,20,36] and on thick aluminum plates. [27,29,32,37] Thus literature on MIG welding on aluminum thin plates in a T-joints configuration lacks the experimental data, which would be fundamental to integrate the Goldak parameters in the existing FE models.

The integration of experiments with numerical simulations can efficiently support a quick evaluation of the welded joints, [18,23,24] evaluating the transient behavior of

the temperature field, the global deformations. The experiments are necessary in order to evaluate the Goldak parameters, which will be included in the TEP analysis.

The aim of the paper is to enlarge the global database to promote the use of thin aluminum sheets in automotive body industries. The MIG welding of 2 mm aluminum plates in T-joint configuration is presented in this paper as a case study, with an integrated approach between numerical model and real metallographic measures. Afterward, the following case studies might be simulated without the experimental part.

II. SIMULATION AND MATERIALS

In this work, Abaqus® FEA tool is exploited to implement the numerical model. As previously described, the simulation has been simplified by two models: the mechanical and thermal model. The mechanical model computes the distortions, whereas the thermal one simulates the welding torch by the Goldak model. The work angle and welding speed are described by Goldak model in an internal subroutine.

The T-joint configuration has been chosen because it is one of the most common joints in automotive chassis design; Figure 2 shows the geometry of the model. Each plate is 100-mm wide, 2-mm thick, and 150-mm long in the joint direction. The two thin plates in the T-joint configuration and the bead are modeled as only one part. The simplification is considered trustworthy since the parts are partially joined by the bead also in the real experiment and their separation during cooling is hindered by fixtures. The welding mask (clamps) is designed to minimize the contact area with the joining

couple, so that the heat losses by conduction are reduced. The clamps mate the parts to each other by blocking their ends. The fixed constraints in Figure 2(a) simulate the clamping during the welding and cooling down phases. The subsequent isostatic state in Figure 2(b) enables the measurement of residual deformations after releasing the T-joint from the fixtures.

The parts were discretized with a mesh of 3D linear brick elements, with an average element dimension of 1 mm. The mesh size amounted to 32,475 elements with 40,812 nodes. The filler material stack was simulated using the death–birth elements technique. [38]

The properties of the bead metal are assumed as being the same as those of the base metal, but the solidus temperature (TS) is decreased at 828.15 K (555°C) to account for dilution. As a matter of fact, TS of base and filler metal alloys is slightly different. The remaining temperature-dependent properties are reported in Figure 3 and Table I. The model accounts for the material heat conductivity with Eq. [2] and for heat transfer in the weld pool, as previously explained.

The effects of properties on the transient temperature, residual deformation, and stress fields in welding simulations have been investigated in previous works, [32] showing that results exhibit errors lower than 10 pct each, approximately. However, the approximations are quite unacceptable if the thermal and mechanical models have to be coupled since it would lead to high errors. Therefore the material heat conductivity k , the Young's modulus E , the coefficient of thermal expansion α , the yield stress σ_Y and the specific heat capacity c_p of the base metal are estimated as linear or

nonlinear temperature functions, as shown in Figure 3 for the base material, in agreement with EN 1999-1-2:2007. [39] However, to simplify the model, some properties with less pronounced temperature dependence are accepted as constant, as reported in Table I, in agreement with literature results. [32] The reported properties are valid for the phenomena occurring in the solid metal. In particular, they are very difficult to evaluate above $0.8 T_S$ of the alloy. [40] For temperatures above T_S the TEP-FE model must take into account for the much higher heat transfer rate through the fluid flow in the weld pool. Taking a practical approach, this multiphase behavior is simulated by increasing at $350 \text{ W/m}^\circ\text{C}$ the material heat conductivity k in Eq. [2] for temperature above T_S . [19]

As an initial condition, $T_0 = 293.15 \text{ K}$ (20°C) was set at all the nodes. The boundary conditions, as Eqs. [3] and [4], are imposed with constant coefficients for convection, $h_f = 2.7 \text{ W/(m}^2 \cdot \text{K)}$, and emissivity, $\varepsilon = 0.9$, on all the external surfaces, in agreement with literature. [41]

The experiments are realized on single fillet welds between two thin aluminum (EN AW-6082-T6) plates in T-joint configuration. This configuration has been selected since the shape complexities of real automotive hollow-extruded struts often do not allow double fillet welds. The filler metal is S-Al-4043, with 1.2 mm diameter. The welding path is 150-mm long in the middle of the T-joint. An example of the T-joint and the set-up realized is shown in Figures 4 and 5. The aim of such experimental activity is to determine the Goldak model parameters, by direct observation of the welded zone.

Robot-assisted welding was used to avoid the human factor variability. MIG welding was performed using a Fronius TransSynergic 4000, using 100 pct Ar at 12 L/ min flow as shielding gas. Electrode stick out was set at 13 mm. Table II lists the set of welding parameters applied. Before welding, the plates were cleaned by a 15 pct vol NaOH aqueous solution. Clamping tools were used to restrain the parts during the welding operation.

Metallurgical measurements were performed both to evaluate the required geometrical information on the welding ellipsoid, as well as to validate the thermal simulation results. A 3D laser scanner, Konica Minolta Range 7, was employed to measure the welding deformations after cooling down for the unclamped component. A matted spray applied onto the sample surface neutralized the high aluminum reflectivity to ease measurements of deformation.

Metallographic specimens, for the determination of the Goldak model parameters were obtained by cutting cross sections of the welded samples, followed by grinding and then polishing with cloths to 1 μ m, using Struers machines. The samples were etched in Keller solution for 20 seconds in order to reveal the microstructure. Metallographic observations were performed by an Olympus SZX 10 stereographic microscope connected to a camera SC30. The weld joint geometries were verified in comparison with the UNI EN ISO 10042:2007 standards.[42] Microhardness tests were performed using 402 MVD micro-Vickers tester, Wolpert W Group, at 500 g load for 15 seconds.

III. RESULTS

The metallurgical measurements on the experimentally welded samples enables to estimate the parameters of the Goldak model, as clarified in Eq. [5] and Figure 6. The parameters a and b come from the evaluation of the shape of the fused zones in a transversal section of the bead, as shown in Figure 6(a), whereas the c_f and c_r come from the final bead area, especially looking at the end crater shape, as shown in Figure 6(b).

The parameters for the double-ellipsoid model, adjusted to match the experiments, are reported in Table III, while the heat flux distribution is shown in Figure 1. Noticeably, the tuned model is intended to reproduce this specific set-up, even if it can also reproduce the general trends of slightly different ones. In the case of a much different set-up, the parameters of the model must be changed by again fitting the simulation and experiments with the explained workflow.

The temperature distribution on the solid model and the comparison between the experimental and numerical result of welding distortion have been shown in Figures 7 and 9, respectively. The transient temperature distribution for the thermal analysis is evaluated on the 3D model surface, as shown in Figure 7(a), and on cross section views, as shown in Figure 7(b). The gray area covers the over-solidus temperature. The simulated temperature field is overlapped with the HAZ-BM boundary, experimentally identified at the sudden drop of the microhardness value from the BM one. The calculated temperatures variation on the HAZ-BM boundary, at points 1 and 2 in Figure 7(a), are reported in Figure 8. The maximum temperatures are, respectively, around 533.15 K to 523.15 K (260°C to 250°C).

Finally, the residual specimen distortions are measured and compared with the simulated ones. The angular distortions are evaluated on consecutive transversal sections which subdivide the specimen in 10 mm intervals along the main direction, as indicated in Reference 35. Figures 9(a) and (b) compare the deformations computed by the simulation with the experimental measures along with their variation range. In sections from 10 to 30 mm, the simulated deformations are slightly higher than the experimental average but still included within the measurements variability, due to edge effect. [33] The experiments and simulations differ by very small errors from 40 to 100 mm. In sections from 110 to 140 mm, the simulated angular deformations slightly overestimate the maximum measured values.

Microhardness path and penetration depth, detected by experimental results, allowed to validate the temperature distribution obtained by simulation. Figure 10(a) shows the microhardness indentation path on the sample at 300 lm distance one after the other (from point 1 towards point 2) and Figure 10(b) reports the resulting microhardness graph. The microhardness profile presents a non-symmetrical behavior due to the T-joint configuration and the consequent dissimilar heat transfer through the plates. In agreement with the literature, the microhardness profile presents three distinct microstructural zones:

- Base material (BM, with hardness ranging from 100 to 105 HV0.5 [43])
- Heat-affected zone (HAZ, with a microhardness presenting a non-linear behavior [43])
- Fusion zone (FZ, with the lowest value of about 50 HV0.5 [27])

The measured microhardness profile is in agreement with the literature results. Close to the FZ, the profile reveals peaks of around 85 HV0.5 due to the resolubilization of the precipitates that occurs for temperatures greater than 773.15 K (500 _____C), and possibly due also to natural aging. The drop of the microhardness to a minimum of 60 to 65HV0.5 and the further increase to the BM value is due to the phase transformations $\beta'' \rightarrow \beta' \rightarrow \beta$ for peak temperatures ranging from 653.15 K to 773.15 K (380°C to 500°C), and $\beta'' \rightarrow \beta'$ ranging from 513.15 K to 653.15 K (240°C to 380°C). [27,43]

The microhardness behavior is confirmed by microstructural studies. Figure 11 shows the microstructure of welding beads at the interface between base metal and fusion zone. The base material microstructure (Figure 11(d)) is different from the fusion zone, where typical wrought structures with non-uniform grain size were detected.

The external zone of the bead close to the base metal (Figures 11(b) and (c)) is characterized by dendritic growth, which corresponds to the zones with higher solidification rate and column-like grains emerged. The microstructure of the inner part (Figure 12(a)) of the fusion zone consists of fine precipitation of a second phase in a solid solution matrix of aluminum, and equiaxial grains were observed. The SEM images confirmed that aluminum solid solution contains Mg₂Si particles; Al-Si eutectic (dark zone Figure 12(a)) is present between the dendrites of the weld bead; and AlMg₂Si eutectic is between the grains of the heat-affected zone.

By image analysis and microhardness profile, the HAZ extension is estimated to amount to about 10 mm. The value is in agreement with simulation result as shown in Figure 7.

The penetration depth, measured on a cooled cross-sectioned sample by optical images, resulted in 0.91 mm, i.e., about 45 pct of the plate thickness. The result is in reasonable agreement with the simulation results, which indicate a fusion zone penetration of 0.7 mm.

Results, with a good agreement between modeled and measured quantities, show that the heat conduction boundary condition can be generally neglected in order to reduce the model computations. However, this approximation is too rough when describing the behavior of the transition ends, where the clamps are in touch with the parts. Also, the shape and volume of the filler metal present higher variability at the first and last contact points.

IV. CONCLUSIONS

The work increases the current database and promotes the use of aluminum in automotive body industries. Since the welding of aluminum thin plates is difficult to control due to high speed of the heat source and high heat flows during heating and cooling, a simulation model could be considered an effective design tool to predict the real phenomena. In literature, there are no data regarding aluminum thin thickness, thus this study provides new data.

The present paper successfully applies an integration method to validate the simulation of the distortion caused by the MIG welding in the case of 2-mm aluminum plates T-joints. The TEP-FE model parameters are identified through experimental tests. The results of the mechanical simulations are comparable with the experimental

measurements along the welding path, especially considering the variability of the process. The results could well predict the welding-induced distortion, which together with local heating during welding must be anticipated and subsequently minimized and counterbalanced.

In the future, a robust parameter design to produce a general design tool will be investigated.

ACKNOWLEDGMENTS

The authors thank Ferrari SpA (Modena, Italy) for its interest, technical contribution, and for the economic support to the present work. The authors thank OMR Automotive SpA (Modena, Italy) for its contribution to the experiments.

REFERENCES

1. W.P. Schmidt, et. al: Int. J. Life Cycle Assess., 2004, vol. 9(6), pp. 405–16.
2. C. Koffler and K. Rohde-Brandenburger: Int. J. Life Cycle Assess., 2010, vol. 15 (1), pp. 128–35.
3. W.J. Joost: JOM, 2012, vol. 64 (9), pp. 1032–38.
4. J.C. Kelly et al.: Environ. Sci. Technol., 2015, vol. 49, pp. 12535–42.
5. M. Cavazzuti et al.: Struct. Multidiscip. Optim., 2011, vol. 44 (1), pp. 45–56.
6. H. Altenbach: Proc. IMechE Part C, 2011, vol. 225 (11), pp. 2481–96.
7. W. Sun et al.: J. Strain Anal. Eng. Design Impact, 2014, vol. 49 (6), pp. 410–20.
8. Mayyas, et al.: Renew. Sustain. Energy Rev., 2012, vol. 16(4), pp. 1845–62.

9. M. Delogu et al.: J. Clean. Prod., 2016, vol. 139, pp. 548–60.
10. N.A. Husain et al.: Proc. IMechE Part C, 2010, vol. 224 (4), pp. 851–61.
11. W.S. Miller et al.: Mater. Sci. Eng. A, 2000, vol. 280 (1), pp. 37–49.
12. M. Rauegi et al.: J. Clean. Prod., 2015, vol. 108, pp. 1168–76.
13. J.F. Tu and A.G. Paleocrassas: J. Mater. Process. Technol., 2011, vol. 211 (1), pp. 95–102.
14. G. Casalino et al.: Mater. Design, 2014, vol. 61, pp. 191–98.
15. J. Hirsh: Trans. Nonferr. Met. Soc. China, 2014, vol. 24, pp. 1995–2002.
16. S. Zhang, P. Zhu, and W. Chen: Proc. IMechE Part C, 2013, vol. 227 (7), pp. 1381–91.
17. S.S. Sabari, et al.: Def. Technol., 2016, vol. 12(4), pp. 324–33.
18. H. Long et al.: Mater. Design, 2009, vol. 30 (10), pp. 4126–35.
19. D. Deng and H. Murakawa: Comput. Mater. Sci., 2008, vol. 43 (2), pp. 353–65.
20. M.J. Attarha and I. Sattari-Far: J. Mater. Process. Technol., 2011, vol. 211 (4), pp. 688–94.
21. R. Wang et al.: Mater. Design, 2009, vol. 30 (9), pp. 3474–81.
22. Y. Liu et al.: Mater. Sci. Eng. A, 2012, vol. 549, pp. 7–13.
23. L. Gannon et al.: Mar. Struct., 2010, vol. 23 (3), pp. 385–404.
24. K. Weman: Welding Process Handbook, CRC Press, Boca Raton, 2003, ISBN: 0849317738, 9780849317736.
25. K. Masubuchi: Analysis of welded structures: residual stresses, distortions and their consequences, Pergamon Press, Oxford, 2006. ISBN: 978-0-08-022714-6.
26. R. Frappier et al.: Sci. Technol. Weld. Joining, 2014, vol. 19 (1), pp. 38–43.

27. F. Lefebvre, S. Ganguly, and I. Sinclair: *Mater. Sci. Eng. A*, 2005, vol. 397 (1), pp. 338–45.
28. N.S. Rossini et al.: *Mater. Des.*, 2012, vol. 35, pp. 572–88.
29. J.F. Ne´lias, et al.: *Int. J. Press.*, 2011, vol. 88(1), pp. 45–56.
30. Y.N., Li, S.M. Xie, J.H. Zhang: *Adv. Mater. Res.*, 2013, vol. 652, pp. 2303–10.
31. D. Deng: *Mater. Des.*, 2009, vol. 30 (2), pp. 359–66.
32. X.K. Zhu and Y.J. Chao: *Comput. Struct.*, 2002, vol. 80 (11), pp. 967–76.
33. Z. Barsoum, et al.: *Procedia Eng.*, 2015, vol. 114, pp. 70–77.
34. J.A. Goldak, M. Akhlaghi: *Computational Welding Mechanics*, Springer, New York, 2005.
35. P. Biswas, M.M. Mahapatra, N.R. Mandal: *Proc. IMechE Part B*, 2010, vol. 224(1), pp. 125–34.
36. G.A. Moraitis and G.N. Labeas: *J. Mater. Process. Technol.*, 2008, vol. 198 (1), pp. 260–69.
37. M.A. Zaeem, M.R. Nami, and M.H. Kadivar: *Comput. Mater. Sci.*, 2007, vol. 38 (4), pp. 588–94.
38. S.E. Chidiac, J.K. Brimacombe, and I.V. Samarasekera: *Appl. Sci. Res.*, 1993, vol. 51 (3), pp. 573–97.
39. EN 1999-1-2, “Eurocode 9: Design of aluminium structures—Part 1–2: Structural fire design,” 2007, European Committee for Standardization, Belgium.
40. C. Schwenk, M. Rethmeier: *Weld. J.*, 2011, vol. 90, pp. 220s–227s. ISSN: 0043-2296, 0096-7629.

41. J.D. Francis: Welding Simulations of Aluminum Alloy Joints by Finite Element Analysis, Thesis Faculty of the Virginia Polytechnic Institute and State University, Master of Science in Aerospace Engineering, 2002, pp. 52–84.
42. UNI EN ISO 10042, 2007, “Welding - Arc-welded Joints in Aluminium and its Alloys—Quality Levels for Imperfections,” Ente Nazionale Italiano di Unificazione, Italy.
43. O.R. Myhr, O. Grong, and S.J. Andersen: Acta Mater., 2001, vol. 49 (1), pp. 65–75.

Figure Captions List

- | | |
|---------|--|
| Fig. 1 | Distribution of the heat flux (a) due to the Goldak double ellipsoidal model (b) (Color figure online). |
| Fig. 2 | Boundary conditions during welding (a) and deformations measurement (b). |
| Fig. 3 | Temperature-dependent material properties (Color figure online). |
| Fig. 4 | Sample T-joint for the simulation and the experiment. |
| Fig. 5 | Experimental set up with the welding robotic system. |
| Fig. 6 | Goldak parameters evaluation from the experiment (a) welding section (b) welding bead. |
| Fig. 7 | Temperature distribution on the solid model (a) and a section normal to welding path (b) (Color figure online). |
| Fig. 8 | Temperature variation with time in points 1 and 2. |
| Fig. 9 | Position of three measurement sections from the specimen end (a) and experimental–numerical comparison (b). |
| Fig. 10 | Sampling path on the specimen (a) and microhardness measurements (b). |
| Fig. 11 | Optical microstructure of welding beads at the interface between base metal and fusion zone. (a) FZ, (b) ZTA, (c) ZTA, (d) BM. |
| Fig. 12 | SEM images of weld joint. |

Table Caption List

Table 1	Constant material properties
Table 2	Welding process parameters for the experiment
Table 3	Goldak parameters of the heat source

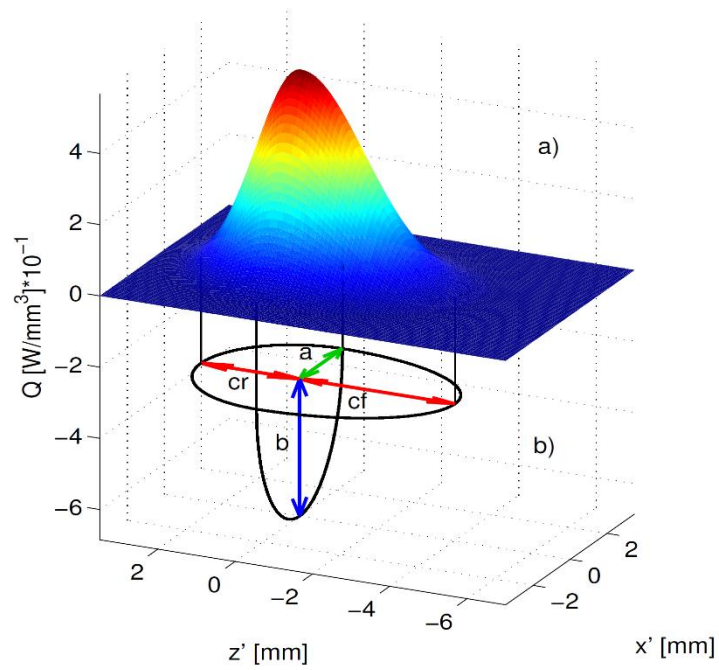
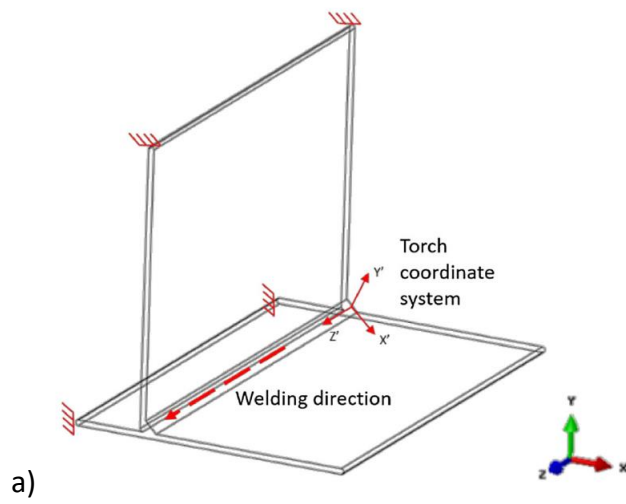
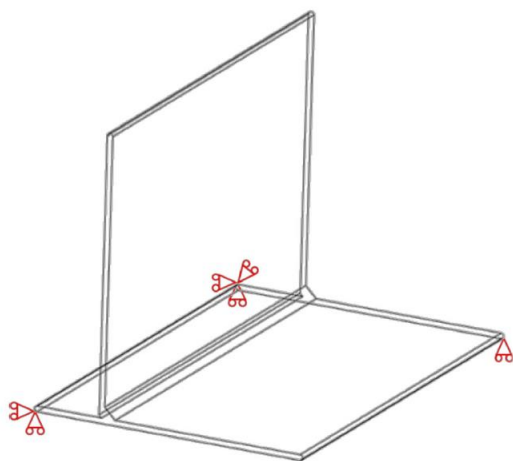


Fig.1





b)
Fig.2

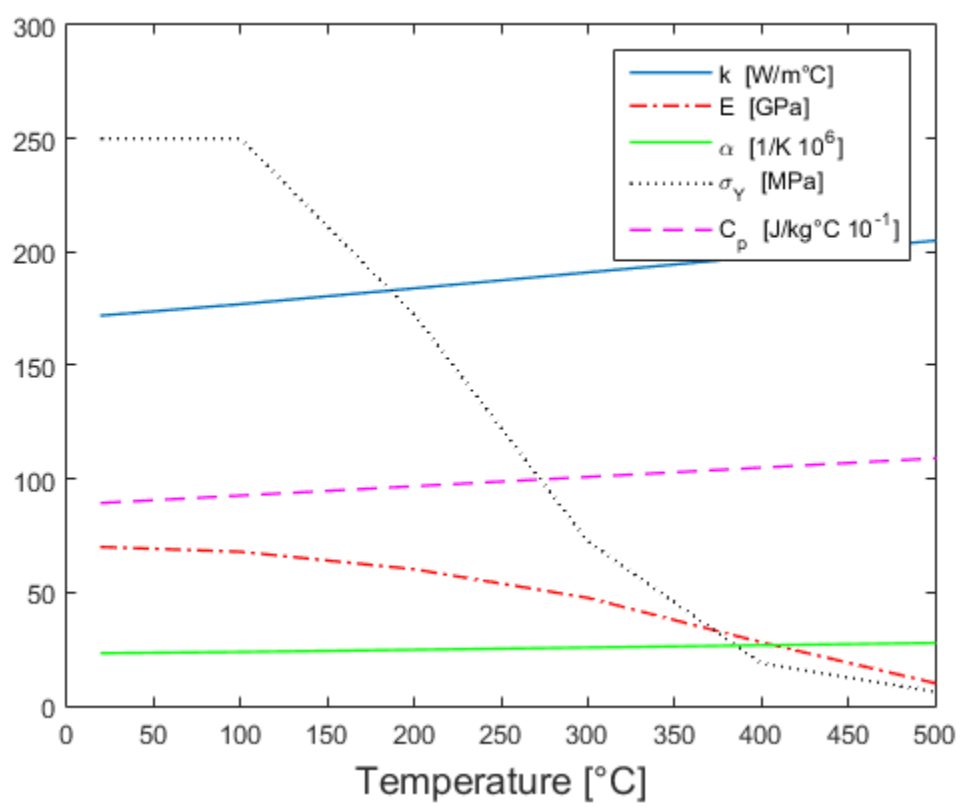


Fig.3

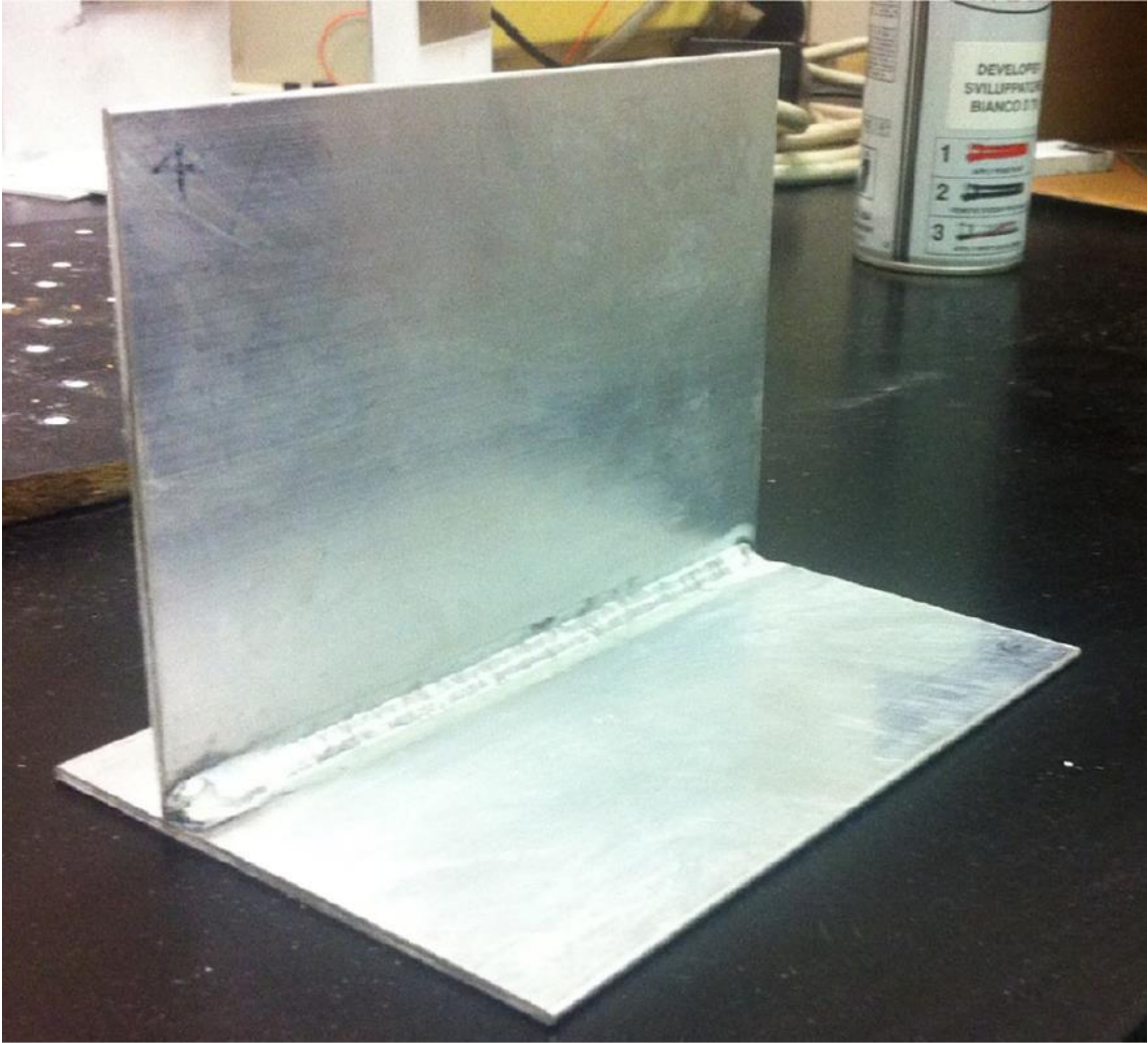


Fig.4



Fig.5

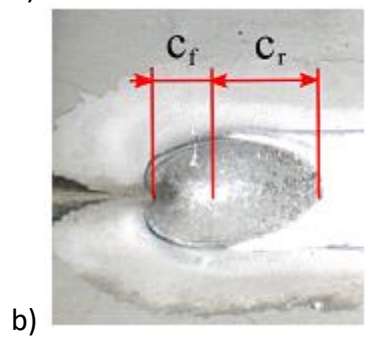
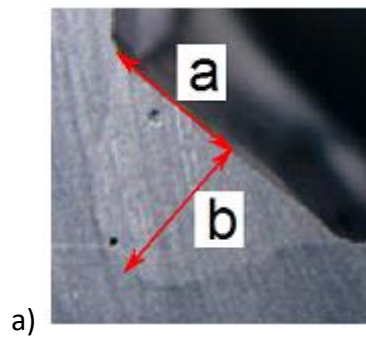
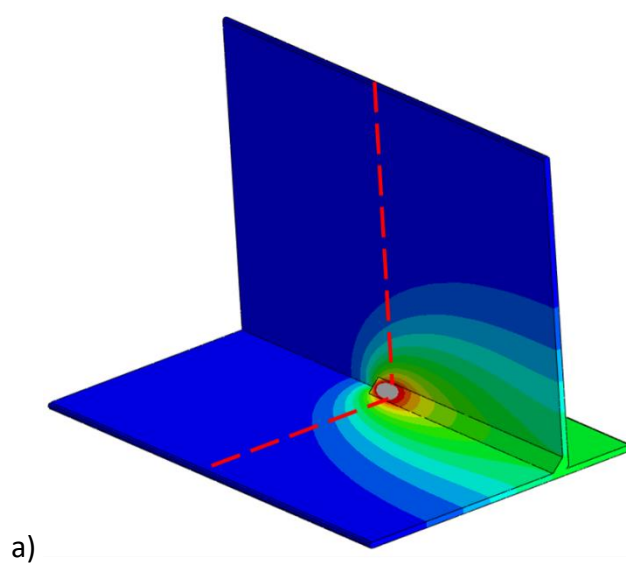
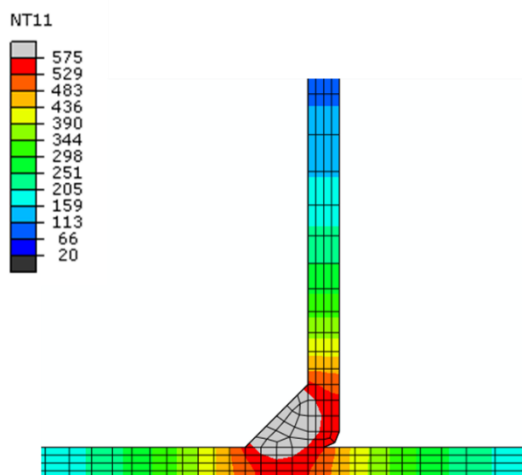


Fig.6





b)
Fig.7

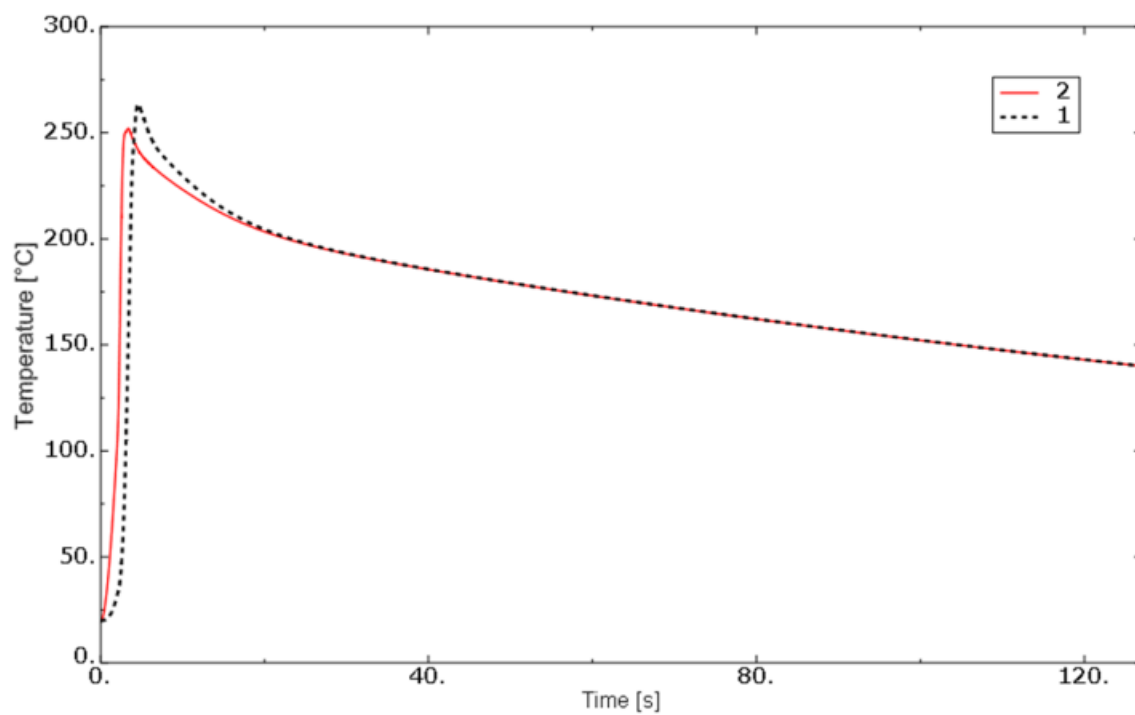
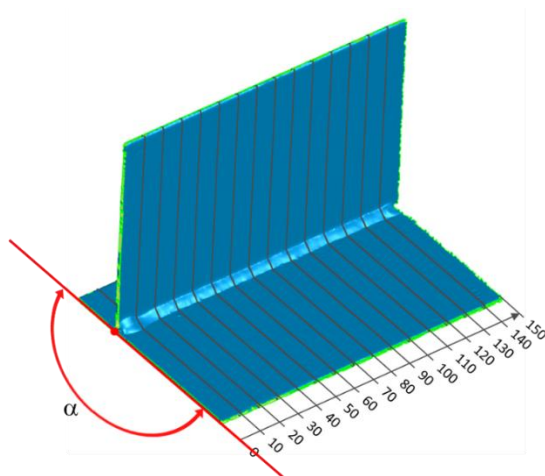
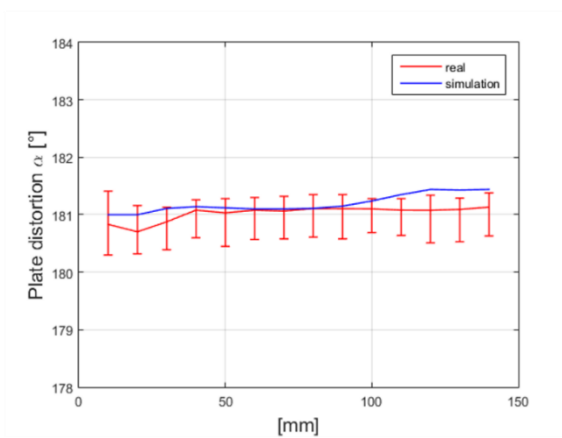


Fig.8



a)



b)

Fig.9

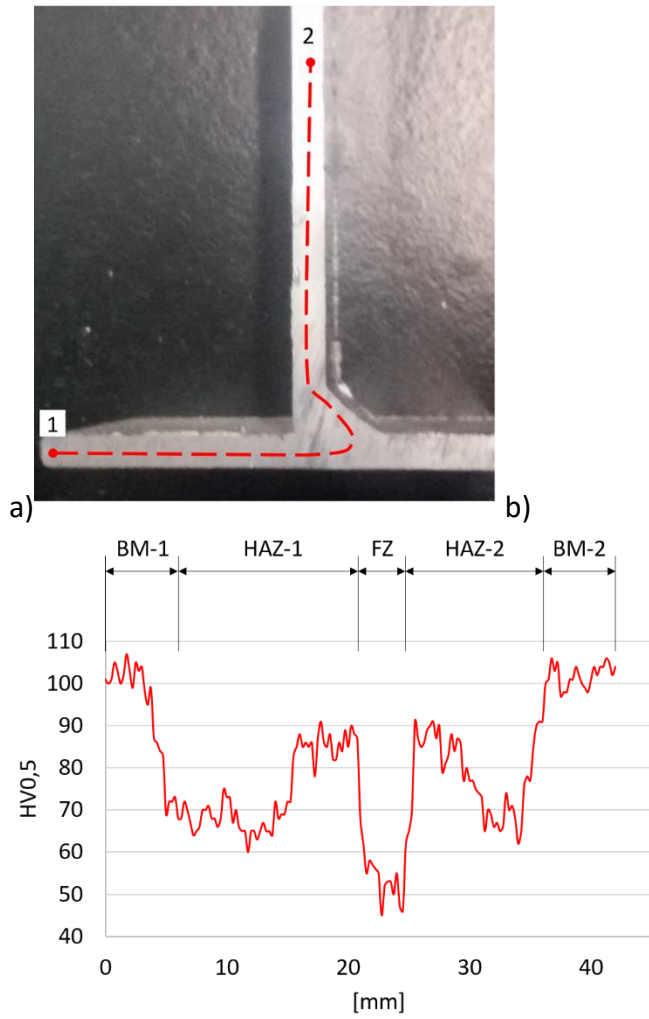
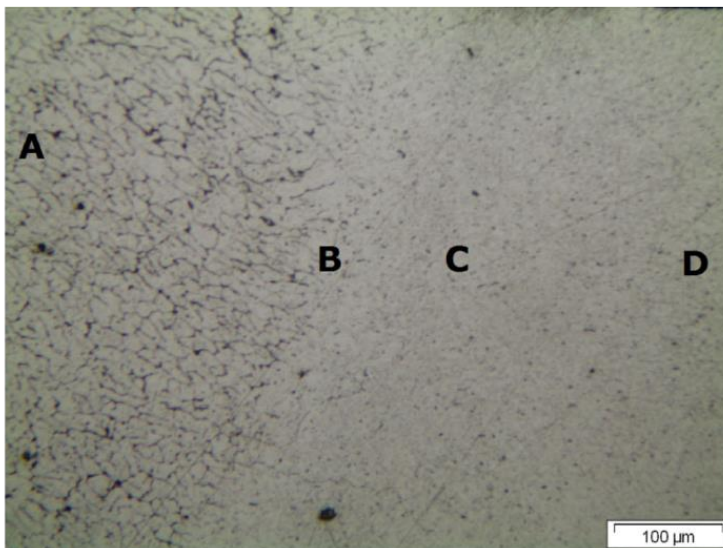
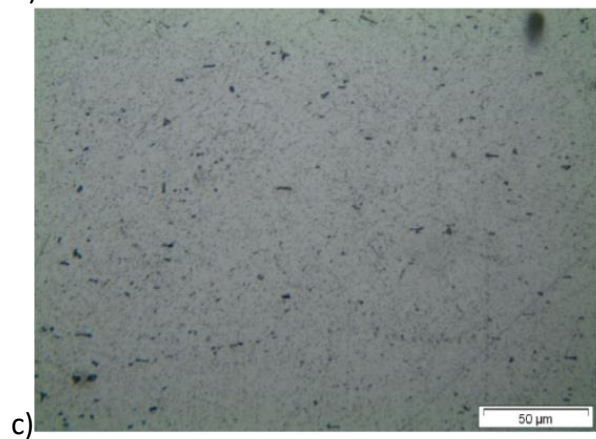
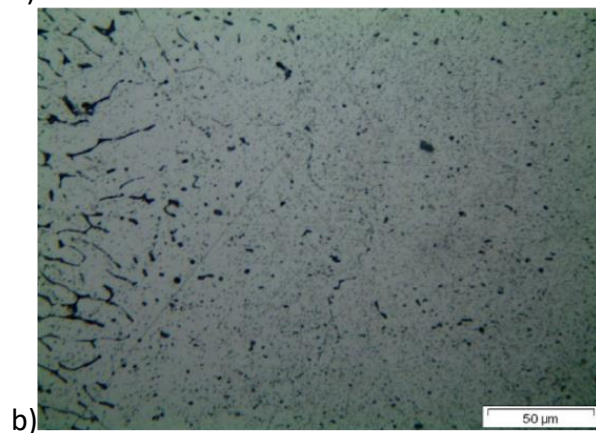
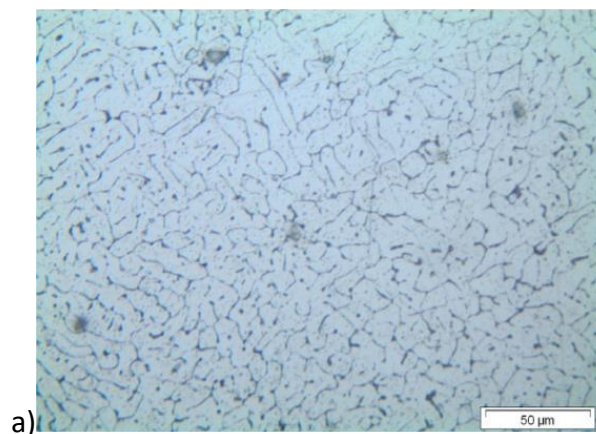
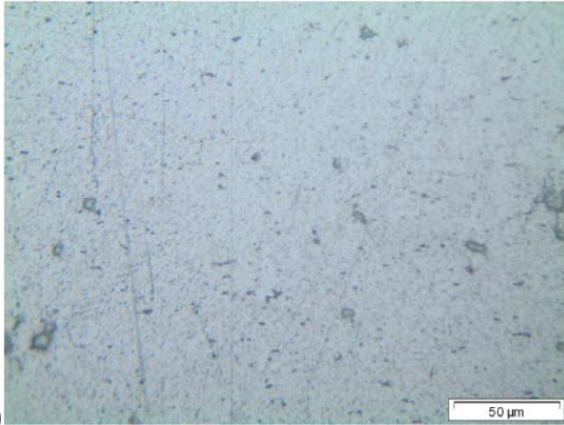


Fig.10

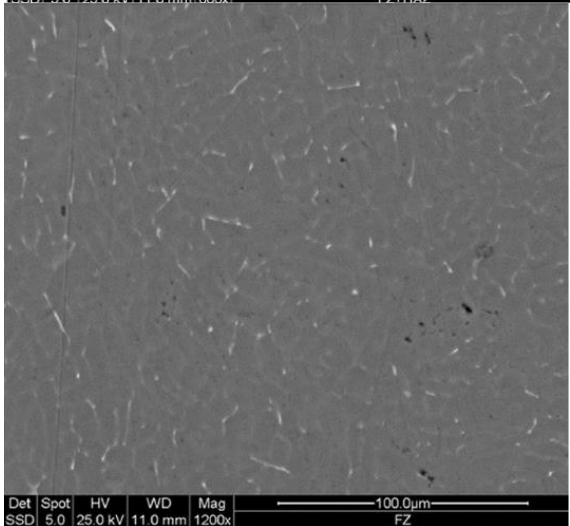
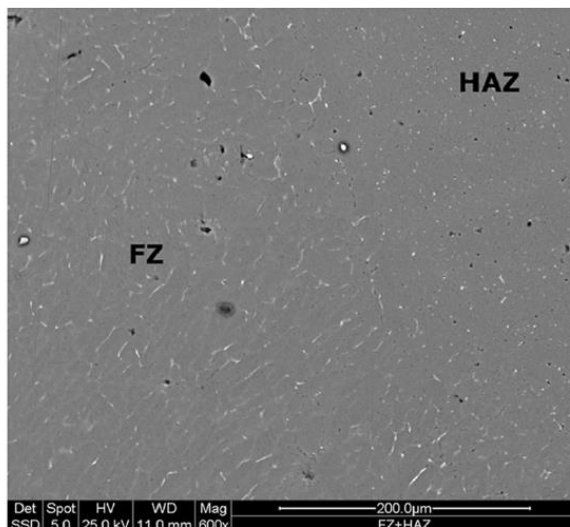






d)

Fig.11



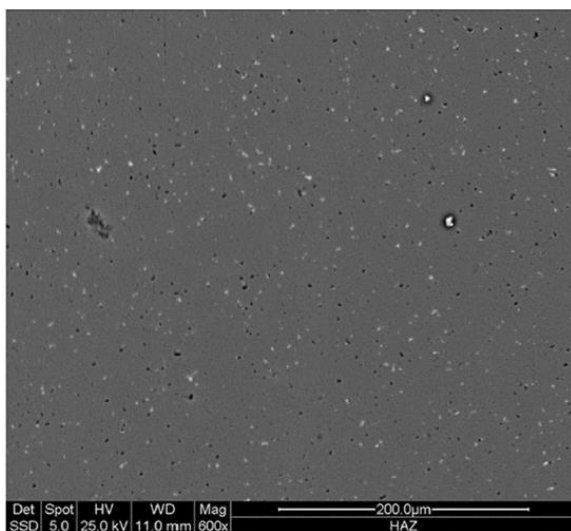


Fig.12

Density P	Latent heat L _f	Solidus temp. T _s	Liquidus temp. T _l	Poisson ratio Y	Emissivity ε
2700kg/m ³	390000kJ/kg	575°C	650°C	0.33	0.3

Welding speed v	Current I	Voltage U	Efficiency H	Wire feed v_{wire}	Wire diameter ϕ_{wire}	Bead length l_{bead}
0.01 m/s	88A	18.8V	80%	0.067m/s	0.0012m	0.15m

a	b	c_f	c_r	f_f	f_f
2.7 mm	2.5 mm	3.0 mm	7.0 mm	0.776	1.224